

<https://doi.org/10.1038/s41612-025-01096-8>

# Persistent millennial-scale glacier fluctuations during the last glacial cycle in the southern Tibetan Plateau

Check for updates

Guocheng Dong<sup>1,2</sup>✉, Weijian Zhou<sup>1,2</sup>✉, Yunchong Fu<sup>1,2</sup>, Feng Xian<sup>1,2</sup> & Li Zhang<sup>1,2</sup>

Determining what was responsible for the last glacial millennial-scale glacier fluctuations can help to pinpoint the causes of abrupt climate events during that period. Yet, the question remains poorly constrained in the Tibetan Plateau (TP), where glaciers react to the global climate system via the northern mid-latitude westerlies and Asian Summer Monsoon (ASM). Here, we examine this issue through <sup>10</sup>Be exposure dating of moraines in the western Nyainqentanglha Mountains, southern TP. We find that glaciers reached their maximum extent during the last glaciation before the Last Glacial Maximum (LGM), and that the LGM termination pre-dated a rapid CO<sub>2</sub> rise at ~18 ka. Changes in summer air temperature, which is tied to the northern tropical Indian Ocean sea surface temperature by the northern mid-latitude westerlies, likely accounted for the pattern of glacial fluctuations, along with the ASM weakening. The rising summer solar insolation from 23 ka also made a positive contribution towards terminating the LGM.

As the most recent glacial cycle, the last ice age featured climate variations on millennial timescales (e.g., stadials and interstadials), as witnessed, for example, by bipolar ice core records<sup>1,2</sup>. Yet, identifying the underlying origin(s) of these millennial-scale climate events remains a fundamental conundrum in paleoclimatology<sup>3</sup>. Mountain glaciers are sensitive to high-frequency climate signals<sup>4</sup>, thereby affording an excellent opportunity of examining the problem<sup>3</sup>. Understanding what was responsible for millennial-scale glacial behaviors is the key step towards addressing the issue.

Holding the largest glacier area outside the polar realms, the Tibetan Plateau (TP) is deemed an ideal region to comprehend glacier dynamics<sup>5</sup>. As such, many efforts have been devoted to establishing high-precision chronologies from moraines deposited by the TP glaciers during the last glaciation<sup>6,7</sup>. Continued progress in chronological control for moraine sequences advances our current knowledge of the last glacial history of TP glaciers. For instance, glaciers attained their maximum extent during the last glacial cycle prior to the Last Glacial Maximum (LGM; 19.0–26.5 ka<sup>8</sup>) in many regions of the TP<sup>9</sup>. Glaciers in the southern TP, which are influenced by the global climate system via the northern mid-latitude westerlies and Asian Summer Monsoon (ASM)<sup>10</sup>, were also limited in extent during the LGM due to arid climate conditions<sup>11–15</sup>. These studies come to the conclusion that glaciers react dynamically to changes in summer air temperature and

precipitation<sup>14,16</sup>. The response of glaciers to millennial-scale climate variations during the last glacial cycle, however, has yet to be fully addressed across the southern TP<sup>9</sup>. Evidence for millennial-scale glacial fluctuations is at best scant, and in most places is absent. Filling the knowledge gaps could help us pinpoint the role of global (e.g., atmospheric CO<sub>2</sub>), hemispheric (e.g., Northern Hemisphere cold stadials), and regional (e.g., ASM precipitation) forcings in millennial-scale glacial events in the TP.

In this study, we explore the last glacial history of glaciers in the Sibiqu catchment, which is located in the southwestern-most part of the western Nyainqentanglha Mountains (WNM; Fig. 1), as a case example of the southern TP for the following reasons: the WNM glaciers are highly sensitive to changes in air temperature<sup>17</sup>; their past fluctuations have the potential to reflect cold stadials<sup>18</sup>; and eight recessional moraines near the outlet of the studied catchment are likely the last glaciation in age from morpho-stratigraphical considerations. Here, we examine these well-preserved glacial deposits through <sup>10</sup>Be surface exposure dating, together with detailed geomorphic mapping. To discuss our results in a broader context, the last glacial history of WNM glaciers was summarized by compiling the newly obtained ( $n=65$ ) and available existing <sup>10</sup>Be data ( $n=75$ ). Potential climate mechanisms behind millennial-scale glacial events were then investigated based on a comparison between the well-established glacial chronologies and a wealth of climate proxy records.

<sup>1</sup>State Key Laboratory of Loess Science, Institute of Earth Environment, Chinese Academy of Sciences, Xi'an, 710061, China. <sup>2</sup>Shaanxi Key Laboratory of Accelerator Mass Spectrometry Technology and Application, Xi'an AMS Center of IEECAS & Xi'an Jiaotong University, Xi'an, 710061, China.

✉ e-mail: [donggc@ieecas.cn](mailto:donggc@ieecas.cn); [weijian@loess.llqg.ac.cn](mailto:weijian@loess.llqg.ac.cn)

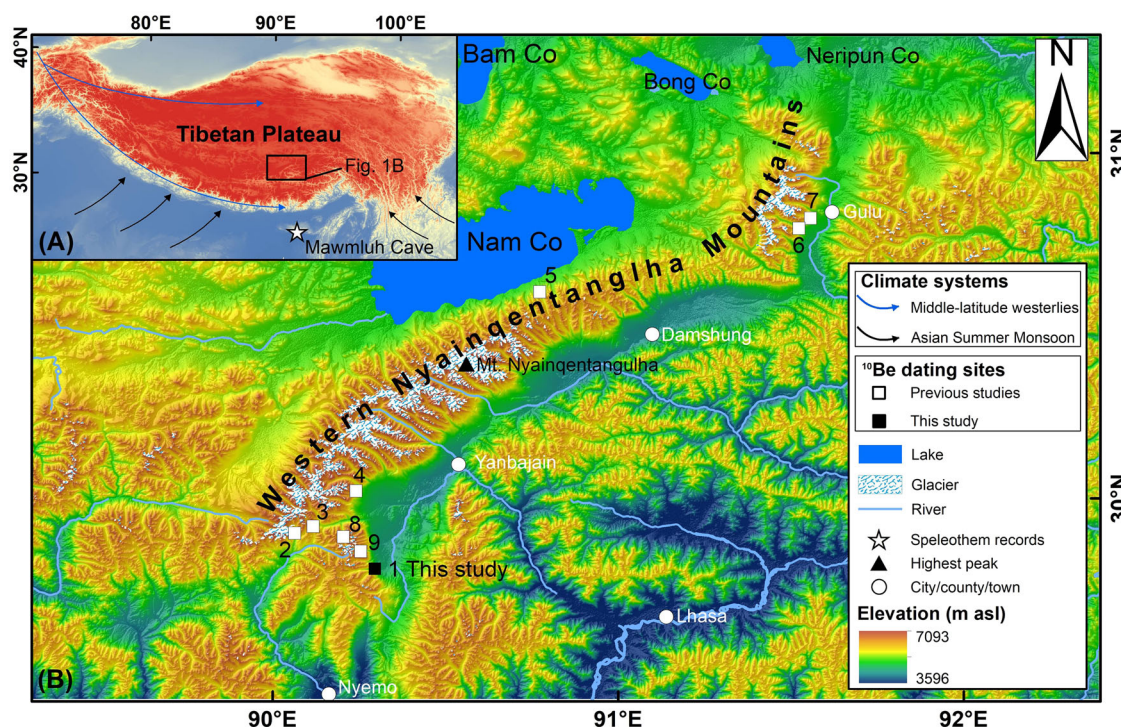


**Fig. 1 | Map showing the location of the study area.** **A** The inset map is an overview of the TP, illustrating the specific location of the WNW. The colored arrows depict the two major climate systems influencing the TP, with blue representing the northern mid-latitude westerlies and black denoting Asian Summer Monsoons<sup>10</sup>. The open asterisk represents the location of Mawmluh Cave. **B** A shaded map

showing the new (black rectangle) and previous (white rectangles) <sup>10</sup>Be dating sites across the whole WNM. 1: the Sibiqu Valley (this study), 2: the Quemuqu Valley<sup>12</sup>, 3: the Pagele Valley<sup>18</sup>, 4: the Ranbuqu Valley<sup>11</sup>, 5: the Payuwang Valley<sup>13</sup>, 6: Barenlong Valley<sup>14</sup>, 7: the Yuqiongqu Valley<sup>11</sup>, 8: the Keqiongqu Valley<sup>69</sup>, and 9: the Taqiongqu Valley<sup>69</sup>. White dots depict the cities and counties around the WNM.

## Results

### Moraine sequences

The geomorphological mapping provides a basis for subdividing the dated glacial features into four main elements, which are defined here, from youngest to oldest, as M1–M4 (Fig. 2). Below, we describe the dated moraines and bouldery ridges following their stratigraphic orders from youngest to oldest.

The two innermost moraine remnants, M1 and M2, are distributed within ~1.4 km outside of the valley confluence (Fig. 2A). These two moraines are characterized by flat surfaces rising ~5–8 m above the present river floor (Supplementary Fig. 1A). Sub-rounded to sub-angular granitic boulders, some exceeding 2 m in height, sporadically occur on moraine surfaces covered with sparse grass (Supplementary Fig. 1A–D).

Immediately outboard of moraine M2, a latero-frontal moraine remnant (M3) extends ~1 km from the mouth of the main valley to the mountain front and terminates at an altitude of ~4560 m above sea level (asl) (Fig. 2B and Supplementary Fig. 1B). This latero-end moraine has a relatively sharp-crested lateral flank, standing as much as 50 m above the surrounding ground, but a forepart featuring flat surface that is mantled with a thin veneer of turf (Supplementary Fig. 1B, E). Scattered on the moraine surface, on which only grass grows, are granitic boulders with a diameter reaching up to 1 m.

The outermost and hence oldest glacial features recognized here are a moraine complex that is composed of five prominent bouldery ridges (Fig. 2 and Supplementary Fig. 1F). These ridges are typically ~1–3 m high and extend as much as ~1.5 km beyond the valley mouth (Fig. 2A). Embedded in or resting on these ridges are granitic boulders reaching ~2 m in height and ~3 m in length. These glacial boulders filled with bright or dark lichen show beige or tan rock varnish on their surfaces (Supplementary Fig. 1F). We informally labeled these five bouldery ridges following arc shape, from youngest to oldest, M4<sub>A</sub>, M4<sub>B</sub>, M4<sub>C</sub>, M4<sub>D</sub>, and M4<sub>E</sub> (Fig. 2). No additional moraine or moraine ridge have been recognized downstream of the M4 moraine assemblage (Fig. 2 and Supplementary Fig. 1G).

### Dating results and moraine ages

Sixty-five boulders sampled on these four sets of moraine remnants examined here yielded apparent <sup>10</sup>Be exposure-ages of  $19.0 \pm 0.5$ – $39.0 \pm 0.8$  ka (Fig. 2 and Supplementary Table 1), with all of which falling squarely into Marine Isotope Stages (MIS) 3 and 2 (Fig. 3)<sup>19</sup>. Most of these ages are in keeping with the relative position of moraines (Fig. 3). Among these ages, fourteen were identified as anomalies by the  $1\sigma$ -level method (Fig. 3), confirmed by the outlier detection results from two other commonly-adopted approaches (Supplementary Fig. 3 and Tables 2 and 3). After rejecting these ages, we use the arithmetic mean of the outlier-free population to represent the age of moraine abandonment. Here, we released both the standard deviation (for local landform comparison) and ‘external uncertainty’ that is calculated by propagating the standard deviation with a production-rate uncertainty (for correlation between glacial records and climate archives).

In doing so, <sup>10</sup>Be exposure-ages within the moraine units follow their stratigraphic order (Figs. 2 and 3). The outermost glacial feature M4<sub>E</sub> has an age of  $35.3 \pm 0.4$  ka ( $n = 5$ ), followed by  $34.1 \pm 0.4$  ka ( $n = 5$ ; M4<sub>D</sub>),  $28.9 \pm 0.9$  ka ( $n = 8$ ; M4<sub>C</sub>),  $25.1 \pm 0.2$  ka ( $n = 9$ ; M4<sub>B</sub>),  $21.6 \pm 0.2$  ka ( $n = 5$ ; M4<sub>A</sub>),  $20.6 \pm 0.1$  ka ( $n = 10$ ; M3),  $20.1 \pm 0.2$  ka ( $n = 4$ ; M2), and  $19.3 \pm 0.3$  ka ( $n = 5$ ; M1).

## Discussion

Despite acknowledging uncertainties in <sup>10</sup>Be ages, we present here a reasonable interpretation of moraine ages based on our current understanding of production rates and scaling models (Supplementary file). Our dating results demonstrate that the studied glaciers culminated at least eight times during the period of ~35–19 ka. The multiple distinct pulses of glacial culminations can be sufficiently differentiated through geomorphologic mapping, together with <sup>10</sup>Be surface exposure dating.

The outermost two bouldery ridges (M4<sub>E</sub> and M4<sub>D</sub>) were dated at  $35.3 \pm 0.4$  ka and  $34.1 \pm 0.4$  ka, suggestive of repeated MIS 3 advances on millennial timescales. No additional moraine remnants have been



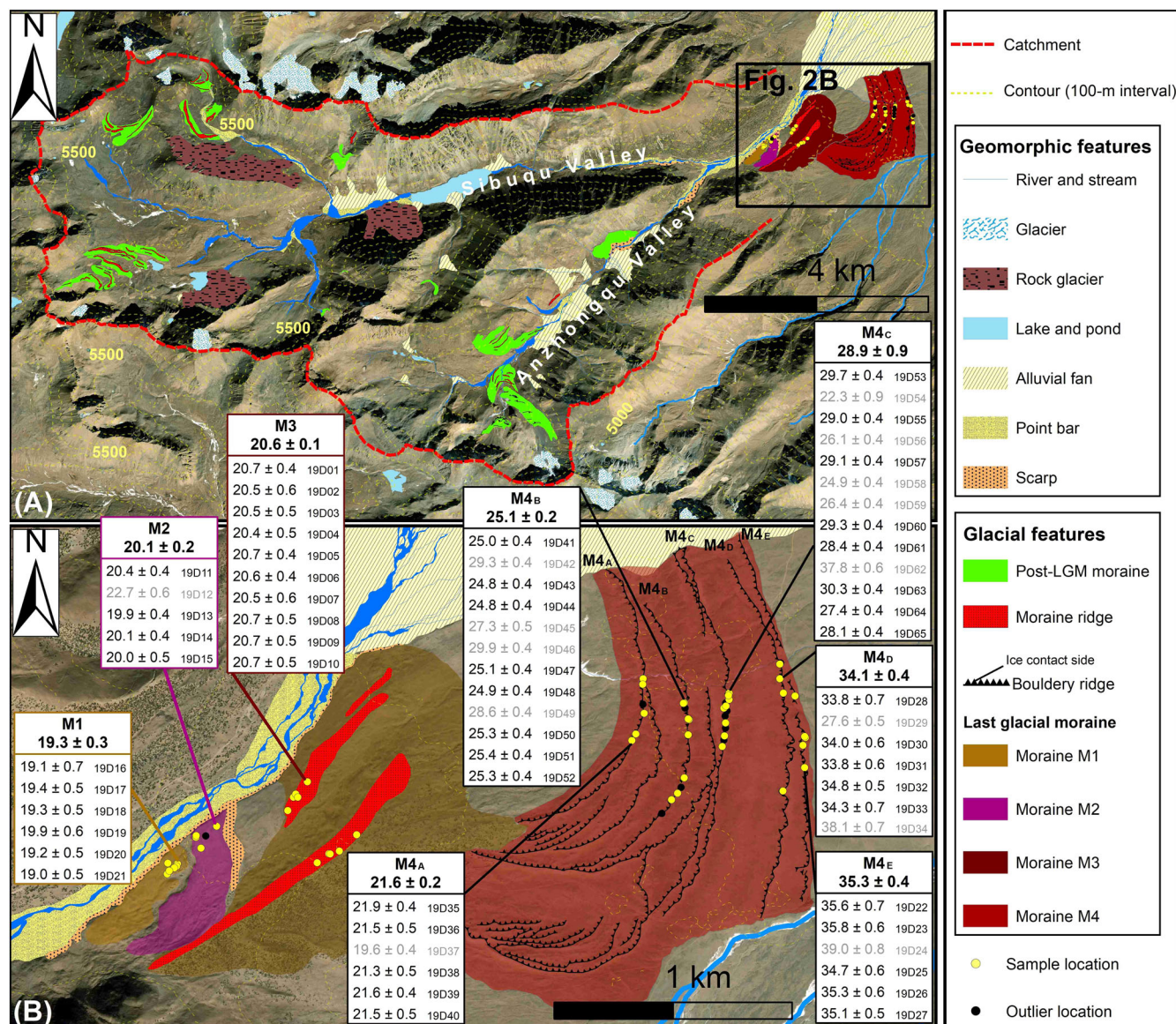


**Fig. 2 | Geomorphological map and exposure ages. A** Geomorphological map showing glacial and associated landforms in the Sibuqu Valley. The red dashed line demarcates the studied catchment. The basemap was derived from ArcGIS online images. **B** Enlarged geomorphological map illustrating the studied moraines along with sample locations and  $^{10}\text{Be}$  exposure-ages (in ka) near the outlet of the Sibuqu

catchment. Black dots indicate potential outliers identified by the  $1\sigma$ -level approach. Exposure ages are reported with their  $1\sigma$  internal uncertainties in the color-coded boxes. Shown at the top of each respective box are moraine names, below which the moraine means are given in ka ( $\pm 1\sigma$  standard deviation).

recognized downstream (Fig. 2 and Supplementary Fig. 1G). That is, glaciers likely achieved their maximum extent of the last glacial cycle during MIS 3, as is often the case in many other mountain ranges on the TP<sup>9</sup>. However, a clear signal of repeated MIS 3 advances is uncommon elsewhere in the TP. A typical example comes from the Mount Jaggang area, central Tibet, where two glacial events were attributed to mid-to-late MIS 3<sup>7</sup>.

The bouldery ridge (M4<sub>C</sub>) preserved immediately upstream was built at  $28.9 \pm 0.9$  ka, meaning that the renewed MIS 2 glacial activity was nearly as extensive as the two MIS 3 advances. Two bouldery ridges (M4<sub>B</sub> and M4<sub>A</sub>) located further up-valley were dated at  $25.1 \pm 0.2$  ka and  $21.6 \pm 0.2$  ka, finding twofold advances in the LGM. The subsequent glacial culmination is also found to accord with the LGM, as indicated by highly-clustered exposure-ages from moraine M3: expressed as mean age, this prominent latero-frontal moraine was emplaced near the valley mouth at  $20.6 \pm 0.1$  ka. Intriguingly, once again, the two following advances, as seen by the  $20.1 \pm 0.2$  ka (M2) and  $19.3 \pm 0.3$  ka (M1) moraines, match well in time with the LGM as well.

Collectively, the MIS 2 glacial maximum was followed by five-phased culminations, with the LGM being the youngest. Of these, the latest four glacial oscillations occurred during the late stage of LGM, supporting the recent findings released in the southeastern TP<sup>20,21</sup>.

No further moraines post-dating  $19.3 \pm 0.3$  ka have been observed within the valley confluence area (Fig. 2 and Supplementary Fig. 1A). Namely, glaciers pulled back into tributary valleys from then on. These suggest that glaciers had not retreated significantly up-valley from the outermost ridge (M4<sub>E</sub>) until  $19.3 \pm 0.3$  ka, signifying that the M1 moraine likely registers the end of the LGM.

Overall, moraine chronologies established here place eight phases of glacial culmination during a period spanning late MIS 3, early MIS 2, and the LGM. The robust glacial chronologies provide, for the first time, convincing evidence of millennial-scale glacial activities during the period in the TP. Such a conclusion is further supported by the estimated response time of glaciers (Supplementary Files), which ranges from 117 yr to 181 yr (Supplementary Fig. 6).

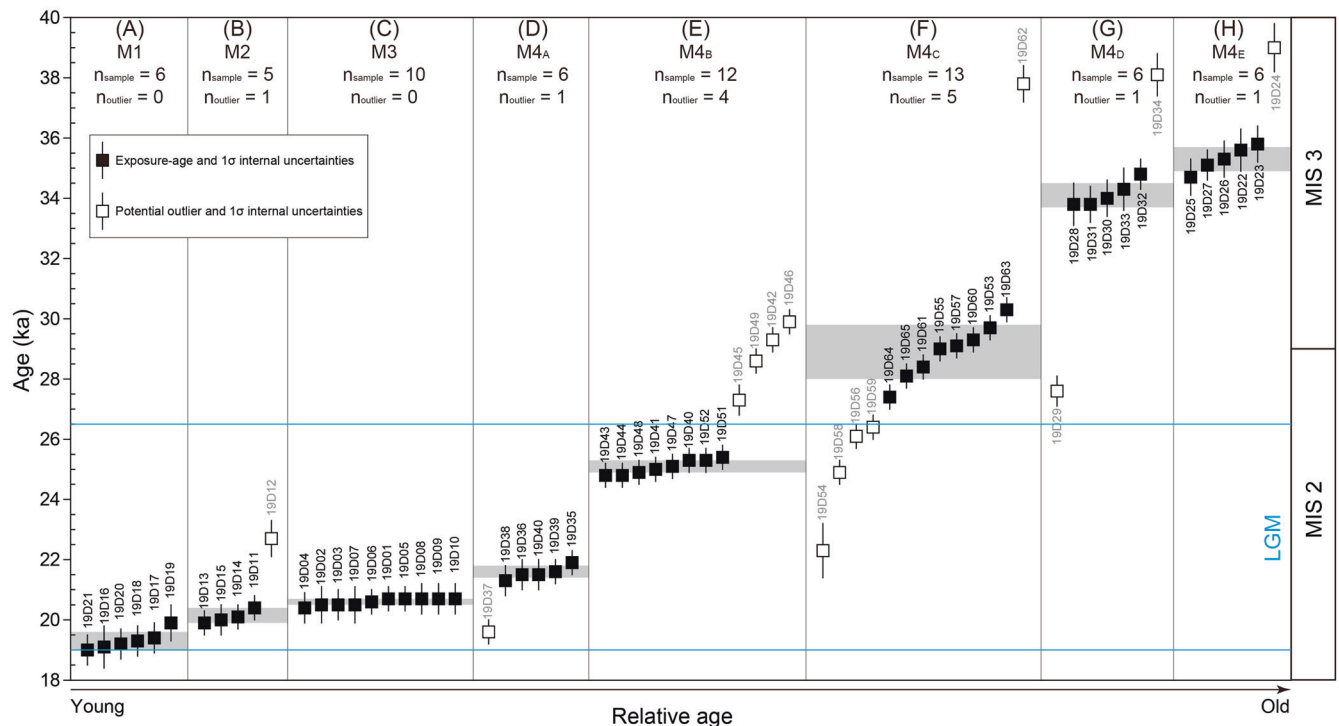


**Fig. 3 | Plots of  $^{10}\text{Be}$  exposure-ages for boulders on moraines and moraine ridges, which are arranged, from youngest to oldest, according to the relative age of glacial deposits.** The individual  $^{10}\text{Be}$  ages and their  $1\sigma$  internal uncertainties are indicated by black rectangles and vertical lines, shown next to which are sample IDs. Open rectangles represent potential outliers identified by the  $1\sigma$ -level strategy. Light

gray horizontal boxes depict the arithmetic mean (with outliers removed) and ‘internal uncertainty’ (standard error). Shown in the right panel are Marine Isotope Stages (MIS) 3 and 2<sup>19</sup>. The LGM (26.5–19.0 ka), displayed by cyan lines, is taken from Clark et al.<sup>8</sup>.

We outline the last glacial moraine chronologies across the WNM based on  $^{10}\text{Be}$  data generated in this and previous studies (Fig. 1B), with the aim of achieving a better understanding of the pattern of last glaciation across this mountain range. To draw a meaningful comparison (Supplementary Fig. 4), we recalculated the existing  $^{10}\text{Be}$  exposure-ages ( $n = 75$ ; Supplementary Table 4) using the same systematics as this study. We followed the original publication to reject potential outliers. We then divided moraines into three quality classes (A–C; Supplementary Fig. 4 and Table 4) following Blomdin et al.<sup>22,23</sup>, aiming to ensure robust correlations between sites based only on the well- (class A) and moderately-clustered (class B) exposure-age groups.

While no evidence of pre-MIS 3 advance has been observed here, five  $^{10}\text{Be}$  ages from a hummocky moraine ( $M_{1b}$ ) outside the Barenlong Valley (site 6 in Fig. 1B) yielded a mean of  $67.4 \pm 9.4$  ka (Supplementary Fig. 4) after removing the oldest age of  $117.9 \pm 3.0$  ka<sup>14</sup>. However, this class B subset remains relatively broad in age range (Supplementary Fig. 4), leaving it an open question whether the WNM glaciers advanced in MIS 4 or an earlier stage. This is also the case elsewhere across the TP and its adjacent mountains<sup>9</sup>.

The finding of MIS 3 moraines ( $M_{4D}$  and  $M_{4E}$ ) suggests that the studied glaciers achieved their maximum extent during the last glaciation at that time, in line with findings presented in the Ranbuqu<sup>11</sup> and Payuwang<sup>13</sup> valleys (sites 4 and 5 in Fig. 1B). This is commonly a scenario in many other mountain ranges on the TP and its surroundings<sup>9</sup>. Yet, the absence of any other MIS 3 moraines that are in class A/B quality (Supplementary Fig. 4) makes it hard to examine the synchronicity of the maximum extent of the last glaciation within the mountain range.

We precisely dated six distinct morainic remnants within MIS 2, with multi-century precision. The new chronological data, together with updated moraine chronologies, enable us to reconstruct the detailed internal structure of MIS 2 in the WNM.

The earliest evidence for a MIS 2 advance comes from the  $M_{4C}$  bouldery ridge. The advance is dated at  $28.9 \pm 0.9$  ka, constraining the MIS 2 glacial maximum to the beginning of the stage (Fig. 3F). Unfortunately, no

class A/B datasets can be correlated with our MIS 2 maximum (Supplementary Fig. 4). Rather, the timing of the two following advances is roughly comparable with chronological data from the Payuwang<sup>13</sup> and Barenlong<sup>14</sup> valleys. This is also the case with the most recent advance found here.

In the Payuwang Valley<sup>13</sup>, fifteen  $^{10}\text{Be}$  dates reported on two moraines near the valley mouth are recalculated to  $20.4 \pm 0.7$ – $40.8 \pm 1.1$  ka (Supplementary Table 2). The inner moraine affords an updated mean age of  $25.5 \pm 3.7$  ka, capturing a glacial event broadly commensurate with our  $25.1 \pm 0.2$  ka advance (Supplementary Fig. 4). Our less extensive  $21.6 \pm 0.2$  ka advance is highly concordant with that reported in the Barenlong Valley<sup>14</sup>, where three recalculated  $^{10}\text{Be}$  ages from moraine  $M_{1a}$  have an arithmetic mean of  $21.8 \pm 0.7$  ka (Supplementary Fig. 4). The unnamed inner moraine from the valley gives a moraine mean of  $18.0 \pm 1.2$  ka, likely contemporaneous with our M1 moraine having a constrained age of  $19.3 \pm 0.3$  ka.

Our M2 and M1 moraines are dated to  $20.1 \pm 0.2$  and  $19.3 \pm 0.3$  ka, which are comparable with those examined in the Quemuqu and Yuqiongqu valleys (sites 2 and 7 in Fig. 1B). Yet, age uncertainties prevent a robust one-to-one correlation (Supplementary Fig. 4). For instance, the inner moraine in the Quemuqu Valley returns a recalculated mean of  $20.4 \pm 0.8$  ka<sup>12</sup> (Supplementary Table 2). Similarly timed glacial advances were determined in the Yuqiongqu Valley, where two moraines provide updated mean ages of  $20.8 \pm 1.4$  ka and  $19.0 \pm 0.9$  ka<sup>11</sup> (Supplementary Fig. 4). Within dating uncertainties, these three moraines are synchronous with our M2 and M1 moraines.

To summarize, the combined analysis of  $^{10}\text{Be}$ -based moraine chronologies reveals that the maximum extent of the last glaciation was indeed before MIS 2, although the regional synchronicity is still far from being fully understood. Apart from the well-known fact, repeated phases of glacial culminations in late MIS 3 and the LGM, are, up to now, limited to the studied catchment. This opens up an unprecedented opportunity to decipher the underlying climatic mechanisms dominating the last glacial history of WNM glaciers.



An often-posed question is whether glacial fluctuations are in response to variations in air temperature or precipitation<sup>9</sup>. In support, many studies propose that the TP glaciers mainly saw changes in summer insolation intensity<sup>24</sup>, ASM intensity<sup>25</sup>, and North Atlantic climates<sup>26,27</sup>. Based on these suggestions, we consider below the potential climate processes related to the millennial-scale glacial events defined here.

The Milankovitch hypothesis<sup>28</sup>, a generally accepted theory, postulates that the development and variation of Pleistocene ice masses were in response to the northern high-latitude summer solar insolation intensity. In this study, however, we note that glacial activities show no consistent relationship with changes in northern high-latitude summer insolation intensity (Fig. 4A, B), as previously suggested for other mid-latitude glaciers<sup>29–31</sup>. Moraines were constructed here during times of minimum, maximum, and

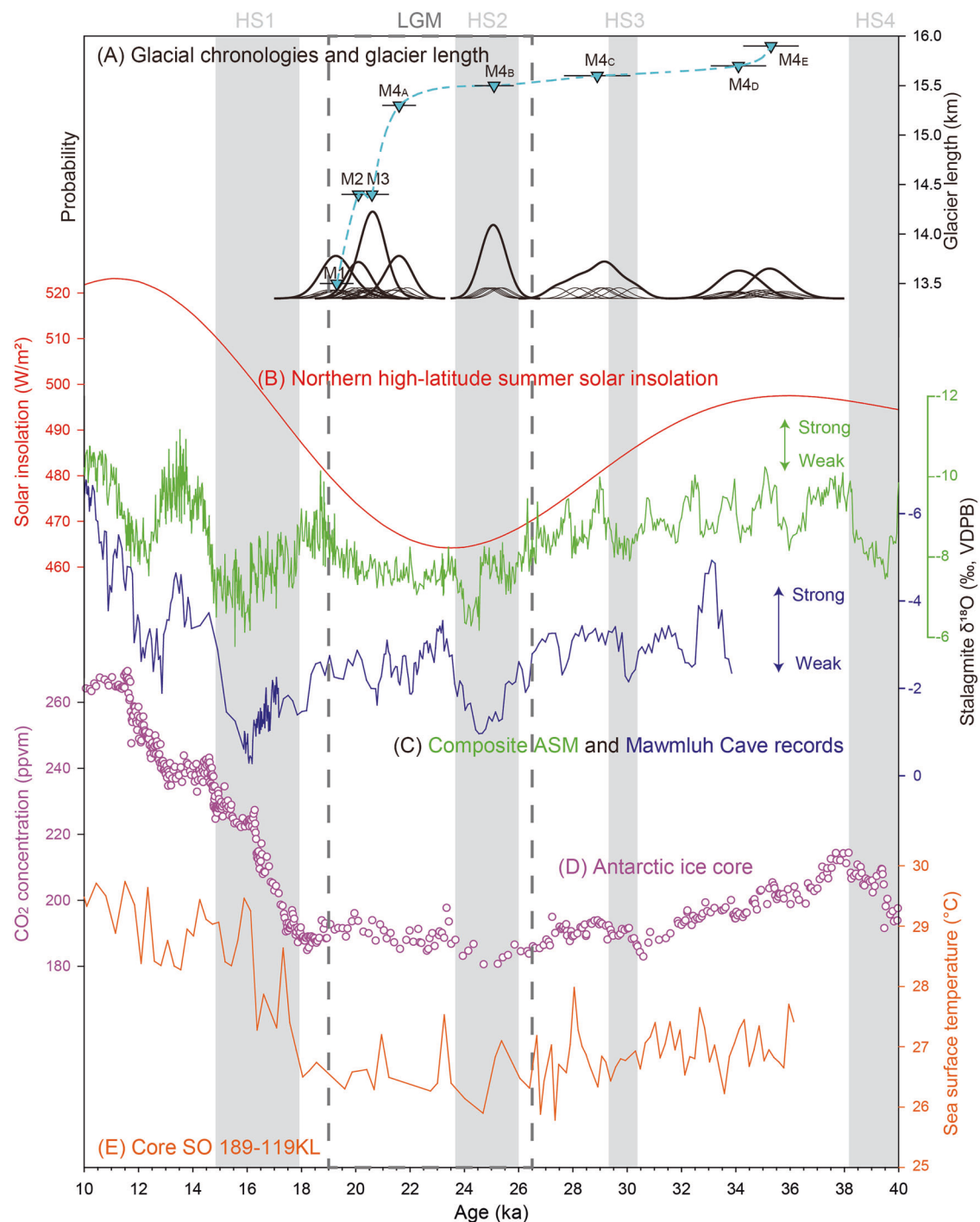


**Fig. 4 | Plot comparing the last glacial history of glaciers in the Sibuqu Valley with climate proxy records mentioned in the text. A** Glacial chronologies and changes in glacier length. Cyan triangles illustrate glacial chronologies, which are determined by the moraine means of outlier-free population. Black horizontal lines exhibit ‘external uncertainty’ that is calculated by propagating the standard deviation of the mean with a production-rate uncertainty of 2.7%<sup>63,64</sup>. Thin black curves are probability density functions (PDFs) of individual <sup>10</sup>Be data, while thick black curves

represent the cumulative PDF of the outlier-free population. **B** Variations in intensity of Northern Hemisphere high-latitude (65°N) summertime (July) solar insolation<sup>32</sup>. **C** Composite ASM records<sup>35</sup> (green) and Indian Summer Monsoon intensity (blue) as reflected by Mawmluh Cave  $\delta^{18}\text{O}$  records<sup>36</sup> from northeastern India (Fig. 1A). **D** A synthesis of atmospheric CO<sub>2</sub> concentrations as measured in Antarctic ice cores<sup>44–46</sup>. **E** The Northern tropical Indian Ocean SSTs reconstructed from core SO189-119KL<sup>47</sup>.

intermediate insolation intensity values<sup>32</sup> (Fig. 4A, B), supporting previous reports in other mid-latitude regions<sup>3,30</sup>. We thus argue that the traditional hypothesis concerning low-frequency forcing on ice-age timescales cannot adequately account for the signal of millennial-scale glacial fluctuations decoded here.

Despite an unsettled question as to the synchronicity of the most extensive advance in the last glaciation, the WNM glaciers were explicitly more restricted in extent during the LGM relative to the early phase of the last glaciation, out of phase with Northern Hemisphere ice sheets. Such a pattern of glacial oscillations has been straightforwardly ascribed to the arid LGM climate<sup>12–14</sup>, which is corroborated by glacier modeling studies in the WNM<sup>33,34</sup>. These studies advocate that monsoon precipitation was highly instrumental in driving MIS 3 advances, building on the pioneering work<sup>24,25</sup>. This prominent deduction is primarily in view of the fact that ASM was more powerful in MIS 3 as compared with MIS 2, as depicted by the composite ASM records<sup>35</sup> and speleothem  $\delta^{18}\text{O}$  records<sup>36</sup> from Mawmluh Cave, northeastern Indian (Fig. 1A) (Fig. 4C). The causal humid environment<sup>37</sup> favored positive glacier mass balance<sup>16</sup> and hence more extensive glaciers in MIS 3<sup>12–14</sup>.

Notwithstanding a broadly accepted notion, it is insufficient to explain millennial-scale glacial records, because most moraines dated here were constructed during weak monsoon conditions (Fig. 4A, C). As a result, Dong et al.<sup>13</sup> posited that the multi-phased last glacial ice expansions likely reflect glacial response to abrupt high-latitude North Atlantic cooling events, predicated on observational evidence that the WNM glaciers are controlled by the mid-latitude westerlies as well<sup>38,39</sup>. Outwardly, the  $35.3 \pm 0.4$  ka and  $34.1 \pm 0.4$  ka advances as seen by M4<sub>B</sub> and M4<sub>C</sub> correspond to Heinrich Stadials (HS) 3 and 2 within the dating uncertainties (Fig. 4A), plausibly supporting such an interpretation. Instead, however, most moraine-building events ( $n=6$ ) are found to fall between the HS events (Fig. 4A), similar to the Mediterranean-wide glacier<sup>40</sup>. Moreover, this finding is not unique to the northern hemisphere. In the Southern Alps of New Zealand, for example, the Pukaki glacier expanded several times between the HS events during MIS 3 and 2<sup>30,41</sup>. This is also the case with the Patagonia Ice Sheet<sup>41</sup>. Whilst more work is needed to exhaustively examine the global fingerprint of such a phenomenon, these findings invite us to revisit the climatic forcing(s) behind millennial-scale glacial fluctuations.

As aforementioned, our geomorphological and chronological data suggest that the M1 moraine likely captures the LGM termination. The greenhouse gases, atmospheric  $\text{CO}_2$  in particular, are traditionally regarded as the principal factor in warming the Earth and hence triggering the near-synchronous inter-hemispheric termination of the LGM<sup>3,42,43</sup>. Intriguingly, however, the rapid and substantial glacial retreat, as marked by M1, outpaces the rapid  $\text{CO}_2$  rise at  $\sim 18$  ka<sup>44–46</sup> (Fig. 4A, D). That is, another heating agent might have been responsible for the end of the LGM defined here.

In this regard, we observe a noteworthy correlation between moraine M1 (Fig. 4A) and sea surface temperatures (SSTs; Fig. 4E) of the Indo-Pacific Warm Pool (IPWP)<sup>47</sup>: a sudden increase in the IPWP SSTs commenced by  $\sim 19.5$  ka (Fig. 4E and Supplementary Figs. 7B–F), coeval with the formation age of moraine M1 (Fig. 4A). Meanwhile, a sharp decline in summer monsoon intensity occurred at that time as well<sup>35,36</sup>, as indicated by the speleothem  $\delta^{18}\text{O}$  records (Fig. 4C). These, along with the sustained rising summer solar insolation after  $\sim 23$  ka<sup>32</sup> (Fig. 4B), likely resulted in a substantial glacial recession that pre-dated changes in atmospheric  $\text{CO}_2$  concentrations.

The earlier glacial fluctuations can also be roughly associated with a decrease of  $\sim 1$ – $2$  °C in the IPWP SSTs (Fig. 4A, E), in particular, with those reconstructed from the northern tropical Indian Ocean (Supplementary Fig. 7A). Several of these associations, although tentative due to age uncertainties, leave open the possibility of a tropical role in the millennial-scale glacial events. As argued by Wang et al.<sup>48,49</sup>, the SST anomaly of IPWP has a profound impact on summer air temperature of, if not the whole, at least the eastern TP. A possible mechanism is that the depressed northern Indian Ocean SST is, at least in part, responsible for a southward migration of the Intertropical Convergence Zone in the Indian Ocean<sup>50,51</sup>. This leads to a

southward displacement of the ascending branch of the Hadley Circulation<sup>52,53</sup>, increasing the strength of the northern Hadley cell<sup>54</sup>. The consequently strengthened Northern Hemisphere subtropical westerly jet<sup>55</sup> delivers the cooling signals in the northern Indian Ocean to the southern TP<sup>48</sup>, accounting for glacial culminations observed here. This provides a feasible explanation for the significant association between SSTs and glacial events, as summer-accumulation type glaciers like those in the WNM<sup>56–58</sup> are quite sensitive to variations in summer air temperature<sup>16</sup>. Changes in the northern Indian Ocean SSTs were likely responsible for the millennial-scale glacial events identified here, while the declining intensity of ASM might have accounted for the stepwise shrinkage of glacier extent during the last glaciation as previously suggested<sup>9</sup>.

To sum up, our new chronological data ( $n=65$ ) indicate that eight geomorphologically distinguishable glacial deposits were formed at  $35.3 \pm 0.4$  ka,  $34.1 \pm 0.4$  ka,  $28.9 \pm 0.9$  ka,  $25.1 \pm 0.2$  ka,  $21.6 \pm 0.2$  ka,  $20.6 \pm 0.1$  ka,  $20.1 \pm 0.2$  ka, and  $19.3 \pm 0.3$  ka. This dataset shows that the most extensive glacial advance during the last glaciation occurred prior to the LGM. Also, these provide, for the first time, convincing evidence that the TP glaciers culminated on millennial timescales during late MIS 3, early MIS 2, and the LGM. We find that the timing of these glacial events tends to correspond with times when SSTs are at minima, if taking age uncertainties into account. Such an association suggests the potential role of northern Indian Ocean SST in driving the observed moraine-forming advances. Yet, such a conclusion remains tentative at present, unless a more precise chronology is established according to a locally calibrated  $^{10}\text{Be}$  production rate and a complete understanding of scaling models.

## Methods

### Geomorphological mapping and sampling

Identification of glacial and associated landforms was initially carried out by using the freely available ArcGIS online images, with the aid of Google Earth images for stereoscopic photo-interpretation. The major categories of geomorphological imprints (e.g., moraines, bouldery ridges, rock glaciers, and meltwater channels) were then mapped on ArcGIS online images (Fig. 2). Ground-truthing was finally conducted to correct the preliminary landform interpretations during field campaigns in June, August, and December 2019.

In order to ensure robust moraine age determination, we sampled five or more granitic boulders well-rooted in the crest of each moraine or bouldery ridge. In total, we collected 65 samples for cosmogenic  $^{10}\text{Be}$  surface exposure dating (Supplementary Table 1). We prioritized large and tall boulders with a height of  $>50$  cm (Supplementary Fig. 1 and Table 1), with the goal of minimizing potential uncertainties in moraine degradation. Rock samples were collected from the uppermost surface of boulders, away from fresh-looking and spallation surfaces, using a hammer and chisel alone or in combination with a Husqvarna K760 circular saw with diamond bit blades. Latitude, longitude, and elevation at the sample locations were recorded using a hand-held Garmin GPS device with an assumed vertical uncertainty of  $\pm 3$  m. Boulder dimensions were also measured, and photographs were taken for all samples and their geologic context (Supplementary Fig. 1).

### $^{10}\text{Be}$ surface exposure dating

Laboratory sample preparation and  $^{10}\text{Be}/^9\text{Be}$  measurements were both implemented at the Xi'an Accelerator Mass Spectrometry (Xi'an-AMS) Center, Institute of Earth Environment, Chinese Academy of Sciences (CAS). Physical and chemical processing of samples was completed following the protocols of Dong et al.<sup>13</sup>, which are modified from Kohl and Nishiizumi<sup>59</sup> and Dortch et al.<sup>60</sup>. Isotopic ratios were then measured relative to the ICN 1-05-4 standardization<sup>61</sup>, with an assigned  $^{10}\text{Be}/^9\text{Be}$  ratio of  $2.851 \times 10^{-12}$ . The measured ratios were converted to  $^{10}\text{Be}$  concentrations in quartz based on blank correction using seven full chemical procedural blanks having a range of  $(1.38\text{--}4.87) \times 10^{-15}$  (Supplementary Table 1). Quartz weights, Be carrier masses, and isotopic ratios are all shown in Supplementary Table 1 as well.

Apparent  $^{10}\text{Be}$  exposure-ages were calculated using Version 3 of the CRONUS-Earth online calculators (<http://hess.ess.washington.edu>)<sup>62</sup>, and using the dataset of  $^{10}\text{Be}$  production-rates calibrated by Fenton et al.<sup>63,64</sup> at the SP lava flow calibration site, North America. We chose this dataset in that the  $^{10}\text{Be}$  production-rate calibration was conducted at the most similar latitude and altitude to our dating site. In this study, we focused on exposure ages derived from the LSDn scaling scheme<sup>65</sup> based on modeled fluxes of cosmic rays. We also reported exposure-ages calculated using the time-dependent and time-independent Lal/Stone scaling models<sup>62,66,67</sup> (Supplementary Table 1). We computed exposure ages assuming a rock density of  $2.7\text{ g/cm}^3$ . We determined topographic shielding using a Python tool, developed by Li<sup>68</sup>, with a combination of the 30-m ASRTM DEM (<http://www.gscloud.cn/>) in the ArcGIS environment with designated  $5^\circ$  intervals in both azimuth and elevation angles. No corrections were carried out for erosion and vegetation or snow cover, in a consistent manner with previous studies<sup>11–14,18,69</sup>. In this way,  $^{10}\text{Be}$  exposure ages reported here should be regarded as minimum estimates.

### Moraine age determination

In order to minimize the spread in ages, we first plotted probability density functions of all exposure-ages using their internal uncertainties (Supplementary Fig. 2). In doing so, we can examine age clusters for each individual exposure-age group, offering help in identifying potential outliers. Anomalies in each dataset were then strictly defined as those exposure-ages that are different than the majority within their  $1\sigma$  internal (analytical) uncertainties (Fig. 3). Also, stratigraphic relationships were considered throughout outlier detection on the basis of field observations. With potential outliers removed, moraine ages were represented by the arithmetic mean. In this study, we reported both the standard deviation of the mean (for local landform comparison) and ‘external uncertainty’ that is calculated by propagating the standard deviation with a production-rate uncertainty of  $2.7\%$ <sup>63,64</sup> (for comparison of glacial records with climate archives).

### Data Availability

No datasets were generated or analysed during the current study.

Received: 29 September 2024; Accepted: 19 May 2025;

Published online: 12 June 2025

### References

1. North Greenland Ice core Project Members. High-resolution record of Northern Hemisphere climate extending into the last interglacial period. *Nature* **431**, 147–151 (2004).
2. WAIS Divide Project Members. Precise inter-pole phasing of abrupt climate change during the last ice age. *Nature* **520**, 661–665 (2015).
3. Denton, G. H. et al. The Zealandia Switch: ice age climate shifts viewed from Southern Hemisphere moraines. *Quat. Sci. Rev.* **257**, 106771 (2021).
4. Oerlemans, J. Extracting a climate signal from 169 glacier records. *Science* **5722**, 675–677 (2005).
5. Yao, T. et al. Third pole environment (TPE). *Environ. Dev.* **3**, 52–64 (2012).
6. Wang, W. et al. Timing and extent of glaciation in northern High-Mountain Asia during the Middle and Late Pleistocene. *Earth Sci. Rev.* **264**, 105089 (2025).
7. Dong, G. et al. The timing and cause of glacial activity during the last glacial in central Tibet based on  $^{10}\text{Be}$  surface exposure dating east of Mount Jaggang, the Xainza range. *Quat. Sci. Rev.* **186**, 284–297 (2018).
8. Clark, P. U. et al. The last glacial maximum. *Science* **325**, 710–714 (2009).
9. Owen, L. A. & Dortch, J. M. Nature and timing of Quaternary glaciation in the Himalayan-Tibetan orogen. *Quat. Sci. Rev.* **88**, 14–54 (2014).
10. Benn, D. I. & Owen, L. A. The role of the Indian summer monsoon and the mid-latitude westerlies in Himalayan glaciation: review and speculative discussion. *J. Geol. Soc.* **155**, 353–363 (1998).
11. Chevalier, M.-L. et al. Constraints on the late Quaternary glaciations in Tibet from cosmogenic exposure ages of moraine surfaces. *Quat. Sci. Rev.* **30**, 528–554 (2011).
12. Dong, G. et al. Cosmogenic  $^{10}\text{Be}$  surface exposure dating and glacier reconstruction for the Last Glacial Maximum in the Quemuqu Valley, western Nyainqentanglha Mountains, South Tibet. *J. Quat. Sci.* **32**, 639–652 (2017).
13. Dong, G., Yi, C. & Caffee, M. W.  $^{10}\text{Be}$  dating of boulders on moraines from the last glacial period in the Nyainqentanglha mountains. *Tibet. Sci. China Earth. Sci.* **57**, 221–231 (2014).
14. Owen, L. A. et al. Climatic and topographic controls on the style and timing of Late Quaternary glaciation throughout Tibet and the Himalaya defined by  $^{10}\text{Be}$  cosmogenic radionuclide surface exposure dating. *Quat. Sci. Rev.* **24**, 1391–1411 (2005).
15. Zhang, Q. et al. Quaternary glaciations in the lopu kangri area, central Gangdise mountains, southern Tibetan plateau. *Quat. Sci. Rev.* **201**, 470–482 (2018).
16. Rupper, S., Roe, G. & Gillespie, A. Spatial patterns of Holocene glacier advance and retreat in Central Asia. *Quat. Res.* **72**, 337–346 (2009).
17. Zhu, M. et al. Differences in mass balance behavior for three glaciers from different climatic regions on the Tibetan Plateau. *Clim. Dyn.* **50**, 3457–3484 (2018).
18. Xu, X. et al. Glacial events during the last glacial termination in the Pagele valley, Qiongmang Gangri peak, southern Tibetan Plateau, and their links to oceanic and atmospheric circulation. *Quat. Res.* **95**, 129–141 (2020).
19. Lisiecki, L. E. & Raymo, M. E. A Pliocene-Pleistocene stack of 57 globally distributed benthic  $\delta^{18}\text{O}$  records. *Paleoceanogr. Paleoclimatol.* **20**, PA1003 (2005).
20. Wang, J. et al. Repeated glacial fluctuations during the Last Glacial Maximum in the southeastern Tibetan Plateau:  $^{10}\text{Be}$  surface exposure dating of moraines in the Lahaku Valley, Haizishan Plateau, China. *Palaeogeogr. Palaeoclimatol. Palaeoecol.* **636**, 111959 (2024).
21. Dong, G., Zhou, W., Fu, Y., Xian, F. & Zhang, L. The LGM termination in the southeastern Tibetan plateau: View from high-frequency LGM glacier fluctuations in the Boshula mountain range. *Quat. Sci. Rev.* **344**, 108971 (2024).
22. Blomdin, R. et al. Evaluating the timing of former glacier expansions in the Tian Shan: a key step towards robust spatial correlations. *Quat. Sci. Rev.* **153**, 78–96 (2016).
23. Blomdin, R. et al. Timing and dynamics of glaciation in the Ikh Turgan Mountains, Altai region, High Asia. *Quat. Geochronol.* **47**, 54–71 (2018).
24. Owen, L. A., Finkel, R. C. & Caffee, M. W. A note on the extent of glaciation throughout the Himalaya during the global Last Glacial Maximum. *Quat. Sci. Rev.* **21**, 147–157 (2002).
25. Shi, Y. & Yao, T. MIS3b (54–44 ka BP) cold period and glacial advance in middle and low latitudes. *J. Glaciol. Geocryol.* **24**, 1–9 (2002).
26. Wang, J. et al. Millennial-scale glacier fluctuations on the southeastern Tibetan Plateau during MIS 2. *Earth Planet. Sci. Lett.* **601**, 117903 (2023).
27. Wang, W., Wang, J., Qiu, J. & Chen, X. Anti-phase glacier fluctuations on the millennial-scale on the southern Tibetan Plateau and New Zealand during the last glacial period. *Quat. Sci. Rev.* **329**, 108565 (2024).
28. Milankovitch, M. *Kanon der Erdbestrahlung Und Seine Anwendung Auf das Eiszeiten-Problem*. (Royal Serbian Academy, Belgrade, 1941).
29. Strand, P. D. et al. A  $^{10}\text{Be}$  moraine chronology of the Last Glaciation and termination at  $49^\circ\text{N}$  in the Mongolian Altai of Central Asia. *Paleoceanogr. Paleoclimatol.* **37**, e2022PA004423 (2022).
30. Strand, P. D. et al. Millennial-scale pulsebeat of glaciation in the Southern Alps of New Zealand. *Quat. Sci. Rev.* **220**, 165–177 (2019).
31. Peltier, C. et al. The large MIS 4 and long MIS 2 glacier maxima on the southern tip of South America. *Quat. Sci. Rev.* **262**, 106858 (2021).



32. Berger, A. & Loutre, M. F. Insolation values for the climate of the last 10 million years. *Quat. Sci. Rev.* **10**, 297–317 (1991).
33. Xu, X. & Glasser, N. F. Glacier sensitivity to equilibrium line altitude and reconstruction for the Last Glacial cycle: glacier modeling in the Payuwan Valley, western Nyaiqentangulha Shan, Tibetan Plateau. *Palaeogeogr. Palaeoclimatol. Palaeoecol.* **440**, 614–620 (2015).
34. Xu, X., Pan, B., Dong, G., Yi, C. & Glasser, N. F. Last Glacial climate reconstruction by exploring glacier sensitivity to climate on the southeastern slope of the western Nyaiqentangulha Shan, Tibetan Plateau. *J. Glaciol.* **63**, 361–371 (2017).
35. Cheng, H. et al. The Asian monsoon over the past 640,000 years and ice age terminations. *Nature* **534**, 640–646 (2016).
36. Dutt, S. et al. Abrupt changes in Indian summer monsoon strength during 33,800 to 5500 years B. P. *Geophys. Res. Lett.* **88**, 159–182 (2015).
37. Herzschuh, U. Palaeo-moisture evolution in monsoonal Central Asia during the last 50,000 years. *Quat. Sci. Rev.* **25**, 163–178 (2006).
38. Yu, W. et al. Different region climate regimes and topography affect the changes in area and mass balance of glaciers on the north and south slopes of the same glacierized massif (the West Nyaiqentangulha Range, Tibetan Plateau). *J. Hydrol.* **495**, 64–73 (2013).
39. Mölg, T., Maussion, F. & Scherer, D. Mid-latitude westerlies as a driver of glacier variability in monsoonal High Asia. *Nat. Clim. Change* **4**, 68–73 (2014).
40. Allard, J. L., Hughes, P. D. & Woodward, J. C. Heinrich Stadial aridity forced Mediterranean-wide glacier retreat in the last cold stage. *Nat. Geosci.* **14**, 197–205 (2021).
41. Kelley, S. E. et al. High-precision  $^{10}\text{Be}$  chronology of moraines in the Southern Alps indicates synchronous cooling in Antarctica and New Zealand 42,000 years ago. *Earth Planet. Sci. Lett.* **405**, 194–206 (2014).
42. Denton, G. H. et al. The last glacial termination. *Science* **328**, 1652–1656 (2010).
43. Schaefer, J. M. et al. Near-synchronous interhemispheric termination of the last glacial maximum in mid-latitudes. *Science* **312**, 1510–1513 (2006).
44. Buizert, C. et al. The WAIS Divide deep ice core WD2014 chronology—Part 1: methane synchronization (68–31 ka BP) and the gas age-ice age difference. *Climate* **11**, 153–173 (2015).
45. Marcott, S. A. et al. Centennial-scale changes in the global carbon cycle during the last deglaciation. *Nature* **514**, 616–619 (2014).
46. Bauska, T. K., Marcott, S. A. & Brook, E. J. Abrupt changes in the global carbon cycle during the last glacial period. *Nat. Geosci.* **14**, 91–96 (2021).
47. Mohtadi, M. et al. North Atlantic forcing of tropical Indian Ocean climate. *Nature* **509**, 76–80 (2014).
48. Wang, C., Yu, L. & Huang, B. The Impact of Warm Pool SST and General Circulation on Increased Temperature over the Tibetan Plateau. *Adv. Atmos. Sci.* **29**, 274–284 (2012).
49. Wang, H., Liu, G., Wang, S. & He, K. Precursory Signals (SST and Soil Moisture) of Summer Surface Temperature Anomalies over the Tibetan Plateau. *Atmosphere* **12**, 146 (2021).
50. Zhou, C., Lu, J., Hu, Y. & Zelinka, M. D. Responses of the Hadley Circulation to regional sea surface temperature changes. *J. Clim.* **33**, 429–441 (2020).
51. Sun, Y., Ramstein, G., Fedorov, A. V., Ding, L. & Liu, B. Tropical Indian Ocean drives Hadley circulation change in a warming climate. *Nat. Sci. Rev.* **12**, nwae375 (2025).
52. Feng, J. et al. Modulation of the meridional structures of the Indo-Pacific warm pool on the response of the Hadley circulation to tropical SST. *J. Clim.* **31**, 8971–8984 (2018).
53. Webster, P. J. *The Elementary Hadley Circulation in The Hadley Circulation: Present, Past and Future* (eds Diaz, H.F. & Bradley, R.S.). 9–60 (2004).
54. Chiang, J. C. H., Lee, S., Putnam, A. E. & Wang, X. South Pacific Split Jet, ITCZ shifts, and atmospheric North-South linkages during abrupt climate changes of the last glacial period. *Earth Planet. Sci. Lett.* **406**, 233–246 (2014).
55. Watt-Meyer, O. & Frierson, D. M. W. ITCZ width controls on Hadley Cell extent and eddy-driven jet position and their response to warming. *J. Clim.* **32**, 1151–1161 (2020).
56. Maussion, F. et al. Precipitation seasonality and variability over the Tibetan Plateau as resolved by the high Asia reanalysis. *J. Clim.* **27**, 1910–1927 (2014).
57. Kang, S. et al. Early onset of rainy season suppresses glacier melt: a case study on Zhadang glacier, Tibetan Plateau. *J. Glaciol.* **55**, 755–758 (2009).
58. Ageta, Y. & Kadota, T. Predictions of changes of glacier mass balance in the Nepal Himalaya and Tibetan Plateau: a case study of air temperature increase for three glaciers. *Ann. Glaciol.* **16**, 89–94 (2017).
59. Kohl, C. P. & Nishiizumi, K. Chemical isolation of quartz for measurement of in-situ-produced cosmogenic nuclides. *Geochim. Cosmochim. Acta* **56**, 3583–3587 (1992).
60. Dortch, J. M. et al. Nature and timing of large landslides in the Himalaya and Transhimalaya of northern India. *Quat. Sci. Rev.* **28**, 1037–1054 (2009).
61. Nishiizumi, K. et al. Absolute calibration of  $^{10}\text{Be}$  AMS standards. *Nucl. Instrum. Methods Phys. Res. Sect. B Beam Interact. Mater.* **258**, 403–413 (2007).
62. Balco, G., Stone, J. O., Lifton, N. A. & Dunai, T. J. A complete and easily accessible means of calculating surface exposure ages or erosion rates from  $^{10}\text{Be}$  and  $^{26}\text{Al}$  measurements. *Quat. Geochronol.* **3**, 174–195 (2008).
63. Fenton, C. R., Binnie, S. A., Dunai, T. & Niedermann, S. 2022. The SPICE project: Calibrated cosmogenic  $^{26}\text{Al}$  production rates and cross-calibrated  $^{26}\text{Al}/^{10}\text{Be}$ ,  $^{26}\text{Al}/^{14}\text{C}$ , and  $^{26}\text{Al}/^{21}\text{Ne}$  ratios in quartz from the SP basalt flow. *AZ, Usa. Quat. Geochronol.* **67**, 101218 (2022).
64. Fenton, C. R., Niedermann, S., Dunai, T. & Binnie, S. A. The SPICE project: Production rates of cosmogenic  $^{21}\text{Ne}$ ,  $^{10}\text{Be}$ , and  $^{14}\text{C}$  in quartz from the 72 ka SP basalt flow, Arizona, USA. *Quat. Geochronol.* **54**, 101019 (2019).
65. Lifton, N., Sato, T. & Dunai, T. J. Scaling in situ cosmogenic nuclide production rates using analytical approximations to atmospheric cosmic-ray fluxes. *Earth Planet. Sci. Lett.* **386**, 149–160 (2014).
66. Lal, D. Cosmic ray labeling of erosion surfaces: in situ nuclide production rates and erosion models. *Earth Planet. Sci. Lett.* **104**, 424–439 (1991).
67. Stone, J. O. Air pressure and cosmogenic isotope production. *J. Geophys. Res.* **105**, 23753–23759 (2000).
68. Li, Y. Determining topographic shielding from digital elevation models for cosmogenic nuclide analysis: a GIS approach and field validation. *J. Mt. Sci.* **10**, 355–362 (2013).
69. Xu, X. et al. The effects of climatic change and inter-annual variability on glacier retreat from ~ 1850s AD moraines in the Kuoqiongongri peak region, southern Tibetan Plateau. *Clim. Dyn.* **62**, 2941–2951 (2023).

## Acknowledgements

This study was supported by CAS "Light of West China" Program (Grant No. XAB2021YN02), the Science and Technology Innovation Project of Laoshan Laboratory (No. LSKJ202203300), the National Natural Science Foundation of China (No. 42071019), the Second Tibetan Plateau Scientific Expedition and Research Program (STEP, 2019QZKK0101), and the Strategic Priority Research Program of Chinese Academy of Sciences (Grant No. XDB40000000). We thank seven anonymous reviewers for their constructive suggestions that greatly improved the paper. We are grateful to Ling Tang from Xi'an Institute for Innovative Earth Environment Research for her help during the fieldwork. We appreciate Pengkai Ding and Jiangying Wu from Xi'an Institute for Innovative Earth Environment Research for their help during laboratory sample processing.



## Author contributions

G.D. and W.Z. conceived the project and led the writing of the paper. F.Y. and F.X. led the laboratory analyses and oversaw the AMS measurements. G.D. led the field work and assisted with laboratory work. L.Z. assisted with laboratory work. All authors contributed to the writing of the paper.

## Competing interests

The authors declare no competing interests.

## Additional information

**Supplementary information** The online version contains supplementary material available at <https://doi.org/10.1038/s41612-025-01096-8>.

**Correspondence** and requests for materials should be addressed to Guocheng Dong or Weijian Zhou.

**Reprints and permissions information** is available at <http://www.nature.com/reprints>

**Publisher's note** Springer Nature remains neutral with regard to jurisdictional claims in published maps and institutional affiliations.

**Open Access** This article is licensed under a Creative Commons Attribution-NonCommercial-NoDerivatives 4.0 International License, which permits any non-commercial use, sharing, distribution and reproduction in any medium or format, as long as you give appropriate credit to the original author(s) and the source, provide a link to the Creative Commons licence, and indicate if you modified the licensed material. You do not have permission under this licence to share adapted material derived from this article or parts of it. The images or other third party material in this article are included in the article's Creative Commons licence, unless indicated otherwise in a credit line to the material. If material is not included in the article's Creative Commons licence and your intended use is not permitted by statutory regulation or exceeds the permitted use, you will need to obtain permission directly from the copyright holder. To view a copy of this licence, visit <http://creativecommons.org/licenses/by-nc-nd/4.0/>.

© The Author(s) 2025